

PASSIVE AND STAR-FORMING GALAXIES AT $1.4 \leq Z \leq 2.5$ IN THE AEGIS FIELD

GUANWEN FANG^{1,2,3}, XU KONG^{1,3,4}, YANG CHEN¹, AND XUANBIN LIN^{1,4}

(Received 2011 April 21; Accepted 2012 March 27)
Accepted for publication in the Astrophysical Journal

ABSTRACT

Using a simple two-color selection based on g -, z -, and K -band photometry, we pick out 1609 star-forming galaxies (sgzKs) and 422 passively evolving galaxies (pgzKs) at $z \sim 2$ from a K -band-selected sample ($K_{AB} < 22.0$) in an area of $\sim 0.44 \text{ deg}^2$ of the All-wavelength Extended Groth Strip International Survey. The number counts of pgzKs in our sample turn over at $K_{AB} \sim 21.0$, and both the number of faint and bright objects (including sgzKs and pgzKs) exceed the predictions of a recent semi-analytic model of galaxy formation, a more successful model is need to explain this diversity. We also find that the star formation rate (SFR) and specific SFR (sSFR) of sgzKs increases with redshift at all masses, implying that star-forming galaxies were much more active on average in the past. Moreover, the sSFR of massive galaxies is lower at all redshifts, suggesting that star formation contributes more to the mass growth of low-mass galaxies than to high-mass galaxies. From *Hubble Space Telescope* Wide Field Camera 3 near-infrared imaging data, we find that morphologies of $z \sim 2$ galaxies not only have diffuse structures with lower G and higher M_{20} values, but also have single-object morphologies (higher G and lower M_{20}), implying that there are morphological variety and different formation process for these galaxies at $z \sim 2$. Finally, we also study the fraction of active galactic nuclei (AGNs) in the gzKs, 82 of 828 gzKs with four IRAC bands can be classified as AGNs ($\sim 10\%$). Most of these AGN candidates have $L_{0.5-10 \text{ keV}} > 10^{41} \text{ erg s}^{-1}$.

Subject headings: cosmology: observations – galaxies: evolution – galaxies: formation – galaxies: high-redshift – galaxies: photometry

1. INTRODUCTION

Understanding when and how the most massive galaxies in the universe formed is one of the most outstanding problems in cosmology and galaxy formation (Conselice et al. 2007). A number of observations suggest that the era of $z \sim 2$ is important in galaxy formation and evolution for various reasons: the cosmic star formation rate (SFR) density begins to drop at $z \sim 2$ from a flat plateau at higher redshifts; the morphological type mix of field galaxies changes remarkably at $z \sim 2$; the number density of QSOs has a peak at $z \sim 2$; $\sim 50\% - 70\%$ of the stellar mass assembly of galaxies took place in the redshift range $1 < z < 3$ (Dickinson et al. 2003; Fontana et al. 2003; Steidel et al. 2004; Kong et al. 2006; Richards et al. 2006; Arnouts et al. 2007; Pozzetti et al. 2007; Noeske et al. 2007). However, in the redshift range $1.4 < z < 3.0$, identifiable spectral features such as Ca II H&K and the 4000 Å break (for passive galaxies) and [O II]λ3727, [O III]λ5007, H α , and H β (for star-forming ones) move out of the optical bands, thus near-infrared imaging and spectroscopy become essential. On the other hand, near-infrared galaxy samples offer several advantages compared to purely optical selections (Cowie et al. 1994). They allow us to select

galaxies at $z > 1$ in the rest-frame optical, correspond more closely to a stellar-mass-selected sample, and are less prone to dust extinction.

There are many ways of using optical and infrared (IR) colors to select the sample of galaxies at $z \sim 2$. A sample of IR-luminous dust-obscured galaxies (DOGs), with a median $\nu L_\nu(8\mu\text{m}) \sim 4 \times 10^{11} L_\odot$, selected to have very red $R - [24]$ color, was recently presented by Dey et al. (2008). From spectroscopic observations DOGs were found to have a tight redshift distribution around $z \sim 2$, very similar to that of the submillimeter-selected galaxies (Chapman et al. 2005). Another different sample, based on near-infrared color selection, is that distant red galaxies with $(J - K)_{\text{vega}} > 2.3$ (DRGs; Franx et al. 2003; van Dokkum et al. 2004). These sources are redder and strong clustering and are believed to be more massive than $10^{11} M_\odot$ (Labbe et al. 2005; Papovich et al. 2006; van Dokkum et al. 2006; Quadri et al. 2008). A third sample uses *Spitzer*/IRAC color to select galaxies at $z > 1.4$. In the redshift range $1.4 < z < 2.7$, the four IRAC bands probe the rest-frame near-infrared bands where galaxy spectral energy distributions (SEDs) have similar shape, thus the IRAC colors are very robust in determining redshift in this range (Farrah et al. 2008; Desai et al. 2009; Huang et al. 2009; Fadda et al. 2010; Fiolet et al. 2010; Fang et al. 2011). Most sources of these samples are starburst-dominated ultraluminous infrared galaxies (ULIRGs; $L_{\text{IR}} > 10^{12} L_\odot$), with an apparent 1.6 μm stellar bump in the IRAC channels.

An independent way to select galaxies at $z \sim 2$ is to use BzK colors. Daddi et al. (2004) introduced a new photometric technique, $BzK = (z - K)_{AB} - (B - z)_{AB} = -0.2$ and $(z - K)_{AB} = 2.5$, for obtaining a virtually com-

¹ Center for Astrophysics, University of Science and Technology of China, Hefei 230026, China; xkong@ustc.edu.cn, wen@mail.ustc.edu.cn

² Harvard-Smithsonian Center for Astrophysics, 60 Garden Street, Cambridge, MA 02138, USA

³ Key Laboratory for the Structure and Evolution of Celestial Objects, Chinese Academy of Sciences, Kunming 650011, China

⁴ Key Laboratory for Research in Galaxies and Cosmology, USTC, Chinese Academy of Sciences, Hefei 230026, China

plete sample of star-forming ($BzK \geq -0.2$) and passively evolving galaxies ($BzK < -0.2$ and $(z - K)_{AB} > 2.5$) at $1.4 \leq z \leq 2.5$. These criteria are reddening independent for star-forming galaxies in the selected redshift range, thus can be used to select the reddest dust-extinguished galaxies. This should allow a relatively unbiased selection of star-forming (sBzKs) and passively evolving galaxies (pBzKs) at $z \sim 2$ within the magnitude limit of the sample studied. Based on *BRIzJK* photometry from Subaru and New Technology Telescope (NTT) over two separate fields, using the *BzK* technique, Kong et al. (2006) have obtained a sample of ~ 500 sBzKs and ~ 160 pBzKs, which were identified over an area of ~ 920 arcmin² to $K_{AB} = 20.8$, of which 320 arcmin² are complete to $K_{AB} = 21.8$. They found that the log of the number counts of pBzKs flattens out by $K_{AB} \sim 20.8$. Similar conclusions were also found by Lane et al. (2007) and McCracken et al. (2010), with much larger samples.

Investigations of the physical properties (i.e., stellar mass, luminosity, size, clustering, SFR, morphology, etc.) of various types of galaxies from high to low redshift are required for better understanding the history of the galaxy formation and evolution. Dunne et al. (2009) studied the star formation history of *K*-selected galaxies in the UKIDSS Ultra-Deep Survey. They found that the specific star formation rate (sSFR) for *K*-selected sources rises strongly with redshift at all stellar masses. In the same field, Williams et al. (2009, 2010) investigated the physical properties (including clustering, size, stellar mass, surface density, SFR, color, etc.) of quiescent and star-forming galaxy populations to $z = 0-2$ with pure photometric data, employing a novel rest-frame $U - V$ versus $V - J$ technique (Wuyts et al. 2007; Wolf et al. 2009; Balogh et al. 2009; Whitaker et al. 2010; Patel et al. 2011). As shown in Figure 8 of Williams et al. (2009) and Figure 2 of Brammer et al. (2011), the red quiescent and star-forming galaxies are found to occupy two distinct population in the rest-frame $U - V$ versus $V - J$ color space. This bimodal behavior is still seen up to $z \sim 2$. At all redshifts, furthermore, massive quiescent galaxies occupy the extreme high end of the surface density distribution and a tight mass-size correlation, while star-forming show a broad range of both densities and sizes. On the other hand, the sizes and surface densities of massive quiescent and star-forming galaxies evolve as simple power-law behavior in $(1 + z)$, with more massive galaxies exhibiting faster evolution. In the meantime, Brammer et al. (2009, 2011), van Dokkum et al. (2010), and Whitaker et al. (2011) provided further evidence for the results above, using the sample from the NEWFIRM Medium Band Survey (NMBS; van Dokkum et al. 2009). More studies for the *K*-selected galaxies have been performed up to $z = 5$ (Cimatti et al. 2002; Abraham et al. 2004; Drory et al. 2005, 2009; Fontana et al. 2006; Pozzetti et al. 2007; Pérez-González et al. 2008; Furusawa et al. 2011).

Morphologies are also essential in studying galaxy mass assembly history and evolution. For the morphologies of galaxies at $z \sim 2$, the traditional Hubble sequence of regular spirals and elliptical galaxies has not settled into place by $z \sim 2$, and a much higher frequency of diffuse, clumpy, and irregular structures is observed among star-forming systems (Lotz et al. 2006; Szomoru et al. 2011). With the advent of *Hubble Space Telescope HST*/Wide

Field Camera 3 (WFC3), it is now possible to obtain a complete rest-frame optical morphological census for massive galaxies at $z \sim 2$.

Understanding the nature of active galactic nuclei (AGNs) and the galaxies that host them is important for such diverse goals as pinpointing the sources of the cosmic X-ray and IR backgrounds and deriving the star formation history of the universe. Multi-wavelength surveys are particularly important for the study of AGNs because their appearance in different wavelength regimes can be quite different. In this work, we will discuss the fraction of AGNs in our sample by using the IRAC band color criteria of Stern et al. (2005) and mid-IR spectral index (Barmby et al. 2006; Park et al. 2010).

To study the physical properties of galaxies in the redshift range $1.4 \lesssim z \lesssim 2.5$, in this paper, we select a sample of passively evolving and star-forming galaxies to $K_{AB} < 22$ in the All-wavelength Extended Groth Strip International Survey (AEGIS) data set. The paper is organized as follows. We describe the multi-band spatial- and ground-based observations of the AEGIS field, and introduce data reduction, photometric redshifts, and method for galaxy sample selection in Section 2. Section 3 presents source number counts (sgzKs and pgzKs). Section 4 presents the physical properties of sgzKs (including the estimate SFR and stellar mass of star-forming galaxies and the stellar mass versus SFR relation). Section 5 describes the morphologies of both sgzKs and pgzKs in the AEGIS. Section 6 discusses the fraction of AGNs in our galaxy sample. Finally, a brief summary is presented in Section 7. All magnitudes and colors are in the AB system unless stated otherwise. Throughout the paper we adopt the following cosmology: $h = H_0[\text{km s}^{-1} \text{Mpc}^{-1}]/100 = 0.71$, $\Omega_\Lambda = 0.73$, $\Omega_M = 0.27$.

2. DATA AND SAMPLE SELECTION

The AEGIS is a collaborative effort to obtain both deep imaging covering all major wavebands from X-ray to radio and optical spectroscopy over a large area of sky ($0.5 - 1.0 \text{ deg}^2$) with the aim of studying the panchromatic properties of galaxies over the last half of the Hubble time. AEGIS is targeted on a special area of the sky, called the Extended Groth Strip (EGS; centered at $\alpha(\text{J2000}) = 14^{\text{h}}19^{\text{m}}12^{\text{s}}$, $\delta(\text{J2000}) = 52^\circ 43' 42''$), which has low-extinction, low-Galactic, and zodiacal infrared emission, has good schedulability by space-based observations, and has therefore attracted a wide range of deep observations at essentially every accessible wavelength over this comparatively wide field (Davis et al. 2007).

2.1. Data Observations

The EGS is a public deep multi-wavelength survey; this field provides an unique combination of area and depth at almost every waveband observable. In this paper, *Chandra*/ACIS X-ray, CFHT/MegaCam Legacy Survey optical, CFHT/CFH12K optical, Palomar/WIRC near-infrared, *Spitzer*/IRAC mid-infrared, and *Spitzer*/MIPS far-infrared imaging data or catalog of the EGS is used. Davis et al. (2007) provided more details on the data reduction and its performance.

For our analysis, specially, the *Chandra*/ACIS DR2 catalog presented by Laird et al. (2009) is used. The X-ray data reduction was performed using the CIAO data

analysis software version 3.3. Basic data reduction proceeded in a manner similar to that described by Nandra et al. (2005). The vast majority of X-ray sources detected in the EGS field are AGNs. In the meantime, the EGS is also one of four 1.0 deg² fields covered by the CFHTLS deep survey (labeled CFHTLS-D3). The data covers the observed wavelength range $3500\text{\AA} < \lambda < 9400\text{\AA}$ in the u^* , g' , r' , i' , z' filters (hereafter labeled u , g , r , i , z). The limiting AB magnitudes is $u \sim 27.0$, $g \sim 28.3$, $r \sim 27.5$, $i \sim 27.0$, $z \sim 26.4$ in the current data set (corresponding to the magnitude limit at 5σ point-source detection). Near-infrared data catalog in J and K bands are available over ~ 0.67 deg² (K -band) with the 5σ magnitudes limits of $J_{\text{AB}} \sim 23.9$ and $K_{\text{AB}} \sim 22.5$ (Bundy et al. 2006). Deep observations of the EGS with *Spitzer*/Infrared Array Camera (IRAC) cover an area of ~ 0.33 deg² to a 50% completeness limit of $1.5 \mu\text{Jy}$ at $3.6 \mu\text{m}$ (Barmby et al. 2008). The catalog comprises 57,434 objects detected at $3.6 \mu\text{m}$, with 84%, 28%, and 24% also detected at $4.5 \mu\text{m}$, $5.8 \mu\text{m}$, $8.0 \mu\text{m}$. As for far-infrared data sets, we also use the *Spitzer*/Multiband Imaging Photometer for *Spitzer* (MIPS) $24 \mu\text{m}$ imaging data with the 5σ flux limit of $\sim 77 \mu\text{Jy}$ over 0.534 deg². Sources are identified and photometry extracted with point-spread function (PSF) fitting using the DAOPHOT software (Stetson 1987).

A catalog of objects with redshifts known from spectroscopic observations is very important to the construction of a photometric redshift code. For this reason, we use the DEEP2 (Deep Extragalactic Evolutionary Probe) spectroscopic data obtained with the Deep Imaging Multi-Object Spectrograph boarded on the Keck 10 m telescope. The DEEP2-DR3 redshift catalog structures contain 24 tags for each object with 50,386 entries in the entire catalog. For the EGS field (DEEP2-field1), we only consider objects with redshift quality greater than or equal to 3. To specifically study the accuracy of the photometric redshift, we also adopt spectroscopic redshifts drawn from the Lyman break galaxy (LBG; $z \sim 3$) catalog of Steidel et al. (2003) and from a small sample of ULIRGs ($z \sim 2$) presented in Huang et al. (2009) and Fang et al. (2011).

The NMBS employs a new technique of using medium-bandwidth near-infrared filters to sample the Balmer/4000Å break from $1.5 < z < 3.5$ at a higher resolution than the standard broadband near-infrared filters (van Dokkum et al. 2009), thereby improving the accuracy of photometric redshifts. A custom set of five medium-bandwidth filters in the wavelength range of $1 - 1.8 \mu\text{m}$ were fabricated for the NEWFIRM camera on the Mayall 4 m telescope on Kitt Peak for the NMBS (see Figure 1 of Whitaker et al. 2011). The survey targets two fields within the COSMOS (Scoville et al. 2007) and AEGIS (Davis et al. 2007) surveys, chosen to take advantage of the wealth of publicly available ancillary data over a broad wavelength range. The more details of the observations, data reduction, and photometry for the survey can be found in Whitaker et al. (2011). The NMBS catalogs contain $\sim 13,000$ galaxies at $z > 1.5$ with accurate photometric redshifts and rest-frame colors. In this paper, we will use their photometric redshifts in the AEGIS field.

2.2. Data Reduction

Source extraction for the CFHTLS optical images is performed with **SExtractor** (Bertin & Arnouts 1996) in the dual image mode (i band is used as the reference image); a $2''$ diameter aperture is used for aperture magnitudes. The edges of the resulting final images, where the signal to noise of CFHTLS/MegaCam images is very low, are trimmed. We finally cross-correlate the i -band catalog (that included u , g , r , and z photometry) with the K -band catalog, with a matching radius $2''$. The final overlapping area of all our data sets is ~ 0.44 deg², and 16,228 objects are included in our final catalog ($K_{\text{AB}} < 22$ mag). Comparing to the NMBS in the AEGIS field (~ 0.21 deg²), we have larger area and more faint galaxies (see Section 2.4). Stellar objects are isolated with the color criterion $(z - K)_{\text{AB}} < 0.4(g - z)_{\text{AB}} - 0.45$, similar as Daddi et al. (2004). A total of 1847 objects are classified as stars, and the number of the final galaxy sample is 14,381. All magnitudes are corrected for Galactic extinction.

2.3. Photometric Redshift

An SED fitting technique based on an updated version of the HyperZ code (Bolzonella et al. 2000) is used to calculate the photometric redshifts (hereafter z_p) for all the $K_{\text{AB}} < 22$ galaxies in the EGS. A set of templates generated by Brammer & van Dokkum (2007) for their EAZY photometric redshift code are used. For each object, the SED derived from the observed magnitudes is compared to each template spectrum in turn, and the weighted mean redshift, computed in the confidence intervals at 99% around the main solution, from HyperZ, is calculated.

To check the accuracy of the photometric redshift we derived, we first compare the z_p with the spectroscopic redshifts. For the 14,381 galaxies in our sample, 2940 of them have spectroscopic redshifts (z_s) from the DEEP2-DR3 redshift catalog, which have a confidence level greater or equal to 97%. In the meantime, spectroscopic redshifts are also available for 35 LBGs at $z \sim 3$ and 14 ULIRGs at $z \sim 2$ within the EGS field (14 ULIRGs presented in Huang et al. 2009 and Fang et al. 2011, 35 LBGs drawn from the catalog of Steidel et al. 2003). In Figure 1(a), we show a comparison of the photometric redshift with the spectroscopic redshift for those 2989 galaxies. Filled triangles and stars correspond to ULIRGs and LBGs with spectroscopic redshifts, respectively. From this figure, we find that our photometric redshifts are in good agreement with the spectroscopic redshifts, with an average $(z_p - z_s)/(1 + z_s) = -0.014$. Only 128 of 2989 galaxies have $(z_p - z_s)/(1 + z_s) > 0.1$; the percentage of catastrophic failures is about 4.3%. The normalized median absolute deviation, σ_{NMAD} , for our galaxy sample is $\sigma_{\text{NMAD}} = 0.032$.

On the other hand, Whitaker et al. (2011) described the full details of the observations, data reduction, and photometry from the NMBS in the AEGIS field (~ 0.21 deg²), also presented a public K -selected photometric catalog along with accurate photometric redshifts and rest-frame colors. For this catalog, we will use their photometric redshifts (z_{NMBS}). We finally cross-correlate our catalog with the NMBS catalog in the AEGIS field, with a matching radius $1''$. A total of 5533 galaxies

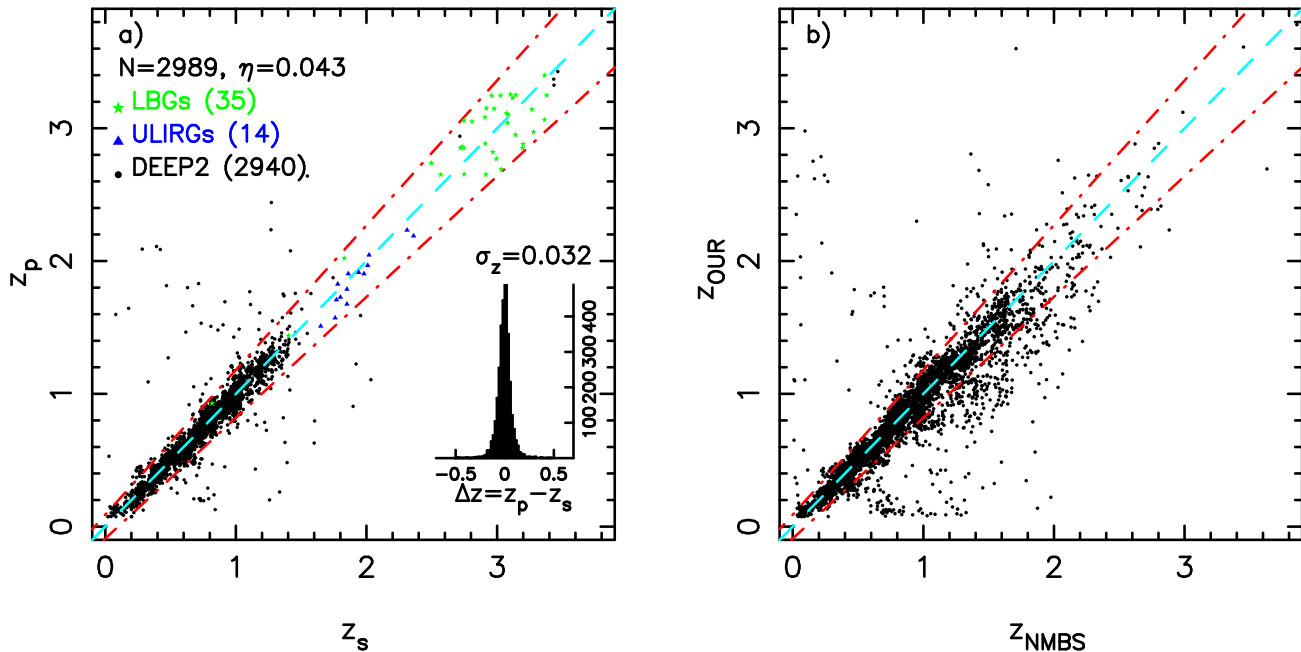


FIG. 1.— (a) Comparison between spectroscopic redshift (z_s) and photometric redshift (z_p). The dot-dashed lines are for $z_p = z_s \pm 0.10(1+z_s)$. The number of galaxies with spectroscopic redshift and the fraction of catastrophic failures ($(z_p - z_s)/(1+z_s) > 0.1$) are listed in the top-left corner. The inset shows the $\Delta z = z_p - z_s$ distribution, and the 1σ dispersion is 0.032. The dashed line is $z_p = z_s$. Filled triangles and stars represent ULIRGs at $z \sim 2$ and LBGs at $z \sim 3$ respectively. Filled circles are drawn from the DEEP2-DR3 redshift catalog. (b) Comparison between z_{NMBS} and z_{OUR} . The z_{NMBS} are drawn from a public K -selected photometric catalog with photometric redshifts in the NMBS/AEGIS field (Whitaker et al. 2011). A total of 5533 galaxies are located in the overlapping area between NMBS and AEGIS.

are located in the overlapping area between NMBS and AEGIS. In Figure 1(b), our photometric redshifts (z_{OUR}) are in good agreement with NMBS photometric redshifts (z_{NMBS}) in the AEGIS field, although there are some large dispersion.

2.4. $z \sim 2$ Galaxy Selection

To select a catalog of objects at $z \sim 2$, we use the BzK selection technique which was introduced by Daddi et al. (2004). This technique has been adopted and tested in several subsequent studies (e.g., Kong et al. 2006; Lane et al. 2007; Blanc et al. 2008; Dunne et al. 2009; McCracken et al. 2010; Onodera et al. 2010; Yoshikawa et al. 2010). To make the comparison possible with previous studies, we wanted our photometric selection criterion to match as closely as possible as the original BzK selection introduced in Daddi et al. (2004). Figure 2(a) shows the transmission profiles of the VLT- BzK filters, which were used in Daddi et al. (2004), the transmission profiles of the CFHT- gz , and the Palomar- K filters of AEGIS, which are used by this paper. From this figure, we find that the shapes of those filters are different. To account for the differences, we carefully compare the stellar sequence in the AEGIS to that of Daddi et al. (2004), with the similar procedure outlined in Kong et al. (2006), and apply small color terms to $B-z$ and $g-z$, $z-K$ in AEGIS and in Daddi et al. (2004), in order to obtain a fully consistent match.

From this analysis, we obtain our new color criteria $g-z$ and $z-K$ to select $z \sim 2$ galaxies: $gzK = (z-K)_{AB} - 1.4(g-z)_{AB} \geq 0.2$ can be used to select $z > 1.4$ star-forming galaxies (hereafter named sgzKs), $gzK < 0.2$ and $(z-K)_{AB} > 2.7$ can be used to isolate $z > 1.4$ passively evolving galaxies (hereafter named pgzKs). To

further elucidate the validity of these gzK criteria, we generate a set of templates, with different star formation history, by Bruzual & Charlot (2003) stellar population synthesis models, and find that galaxies at $1.4 \lesssim z \lesssim 2.5$ with ongoing star formation indeed lie in the $gzK \geq 0.2$ region as expected, passively evolving galaxies lie in the $gzK < 0.2$ and $(z-K)_{AB} > 2.7$ region of the $g-z$ and $z-K$ diagram.

Figure 2(b) shows the gzK color diagram of K -selected objects in the AEGIS. Using the color criterion $gzK = (z-K)_{AB} - 1.4(g-z)_{AB} \geq 0.2$ (the black solid line), 1609 galaxies with $K_{AB} < 22$ are selected as sgzKs (blue squares), which occupy a narrow range on the left of the solid line in Figure 2(b). Using $gzK < 0.2$ and $(z-K)_{AB} > 2.7$ (dot-dashed line), 422 objects are selected as candidate pgzKs (red circles), which lie in the top-right part of Figure 2(b). The sample of gzK s (pgzKs and sgzKs) with open circles from the overlapping area between NMBS and AEGIS. These gzK s mostly lie along the boundary with non- gzK objects, comparing to the photometric redshift distribution for gzK s in our sample, their photometric redshifts have lower values. The surface density of $K_{AB} < 22$ sgzKs + pgzKs is $\sim 1.28 \text{ arcmin}^{-2}$, which is in good agreement with those presented in Daddi et al. (2004), about $\sim 1.1 \text{ arcmin}^{-2}$, and Kong et al. (2006), about $\sim 1.4 \text{ arcmin}^{-2}$.

In Figure 3(a), we show the histogram of the photometric redshift for all K -selected galaxies in our sample. To check how efficient is our gzK color criteria in singling out $z > 1.4$ galaxies, the cross-hatched region shows all non- gzK galaxies in our sample. From this figure, we find that only 4% of galaxies with photometric redshift $z > 1.4$ cannot be selected by the gzK color criteria, which means the gzK criteria are quite efficient in sin-

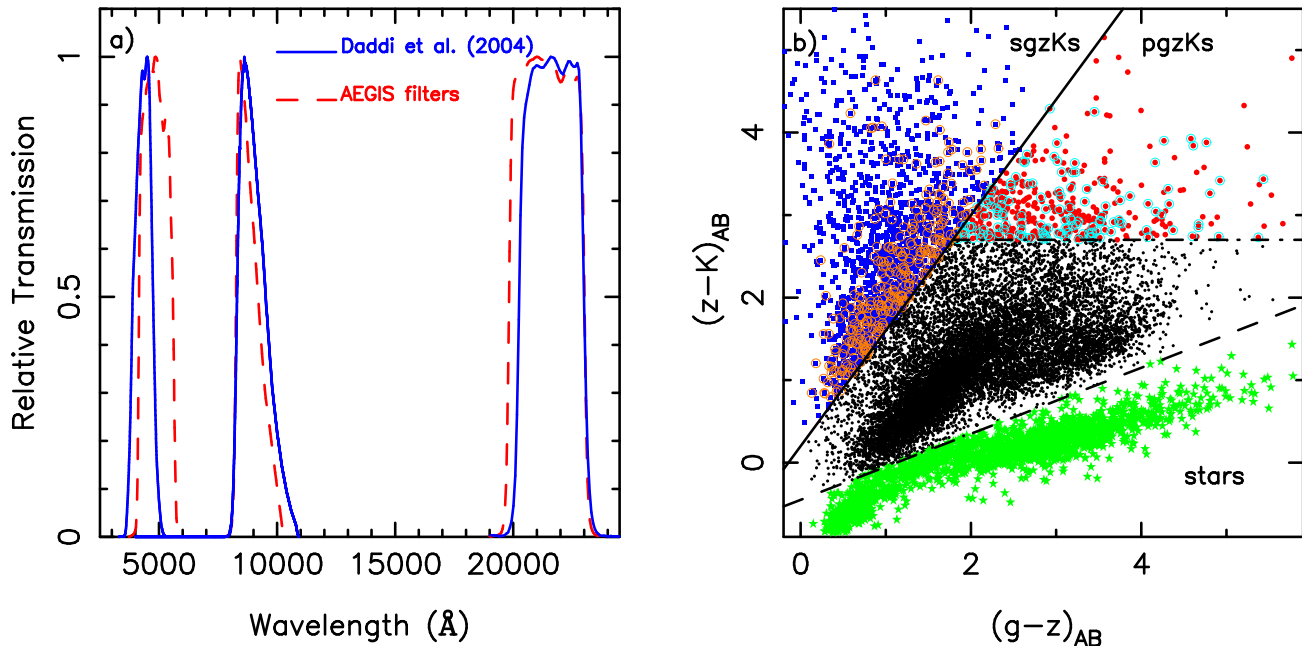


FIG. 2.— (a) Filter transmission profiles for the AEGIS and those used by Daddi et al. (2004). These profiles are normalized to a maximum throughput of 1. The solid lines correspond to the B -, z -, and K_s -band filter curves used in Daddi et al. (2004), respectively; the dashed lines correspond to the g -, z -, and K -band curves used in the AEGIS. (b) Two-color $(z-K)_{AB}$ vs. $(g-z)_{AB}$ diagram for the galaxies in the EGS field. Galaxies at high redshifts are highlighted. The diagonal solid line defines the region $gzK = (z-K)_{AB} - 1.4(g-z)_{AB} \geq 0.2$ that is efficient to isolate $z > 1.4$ star-forming galaxies (sgzKs). The horizontal dot-dashed line further defines the region $(z-K)_{AB} > 2.7$ that contains old galaxies at $z > 1.4$ (pgzKs). The dashed line defines the region occupied by stellar objects. Filled stars show stellar objects in our fields with $(z-K)_{AB} - 0.4(g-z)_{AB} < -0.45$; filled squares represent sgzKs; filled circles represent pgzKs. The sample of gzKs (pgzKs and sgzKs) with open circles from the overlapping area between NMBS and AEGIS. These gzKs mostly lie along the boundary with non-gzK objects; comparing to the photometric redshift distribution for gzKs in our sample, their photometric redshifts have lower values.

gling out high-redshift galaxies. Figure 3(b) shows the distribution of the photometric redshifts of sgzKs, with a median value $z \sim 1.8$. Most of them have redshifts at the range $1.4 \leq z \leq 2.5$, only 8.5% of them with $z < 1.4$ and 8.3% with $z > 2.5$. We show the redshift distribution of pgzKs in Figure 3(c); it clearly shows that there is a considerable fraction (12.8%) of objects at low redshift ($z < 1.0$). The median redshift value of pgzKs is ~ 1.5 , which is similar to that ($\bar{z} \sim 1.4$) of McCracken et al. (2010).

3. NUMBER COUNTS OF GZKS

Figure 4 shows the differential number counts of sgzKs (left panel) and pgzKs(right panel). In both panels of Figure. 4, results from the Deep3a-F (asterisks) and Daddi-F (open diamonds) from Kong et al. (2006), UKIDSS (open squares, Lane et al. 2007; crosses, Hartley et al. 2008), MUSYC (open triangles, Blanc et al. 2008), and COSMOS (open circles, McCracken et al. 2010) are also plotted for comparison. Figure 4(a) shows the number counts of sgzKs, no correction for incompleteness is applied to our data. As shown in the figure, our number counts of sgzKs in the EGS field are in good agreement with the number counts of $z \sim 2$ star-forming galaxies in Kong et al. (2006), Blanc et al. (2008), and McCracken et al. (2010). However, the counts presented by Lane et al. (2007) are offset compared to our counts, which is also found by McCracken et al. (2010), and the cause for this discrepancy may arises from an incorrect transformation to Daddi et al. ’s (2004) filter set in Lane et al. (2007).

Figure 4(b) shows the number counts of pgzKs. Our

number counts of pBzKs, in general, are in good agreement with those presented in the literature for $z > 1.4$ passively evolving galaxies. At bright magnitudes (e.g., $K_{AB} < 21.0$) our counts are in very good agreement with the pBzKs counts from McCracken et al. (2010). However, the number counts of ours and those of McCracken et al. (2010) are slightly below those from Blanc et al. (2008) at faint magnitudes. Combining literature data with the present work, we can examine the global shape of the $z > 1.4$ passively evolving galaxy counts over a very wide dynamic range. This strongly suggests a break feature in the slope at $K_{AB} < 21.0$, which was found in Kong et al. (2006) already.

The dot-dashed lines in Figure 4(a) and (b) show the number counts from the semi-analytic model of Kitzbichler & White (2007). The number counts of quiescent galaxies and star-forming galaxies were derived by McCracken et al. (2010), following the approach of Daddi et al. (2007). From Figure 4, we find the models overpredict the number of faint galaxies, but underpredict the number of bright galaxies in all two plots. Given the narrow redshift range of our $z > 1.4$ galaxy population, apparent K magnitude is a good proxy for absolute K magnitude, which can itself be directly related to underlying stellar mass (Daddi et al. 2004). This implies that these models predict too many small low-mass star-forming and passively evolving galaxies, and too few large high-mass star-forming and passively evolving galaxies at $z > 1.4$. Similar conclusions were drawn by Fontana et al. (2006) and McCracken et al. (2010). Therefore, models incorporating AGN feedback similar to Kitzbichler & White underpredicted the number of

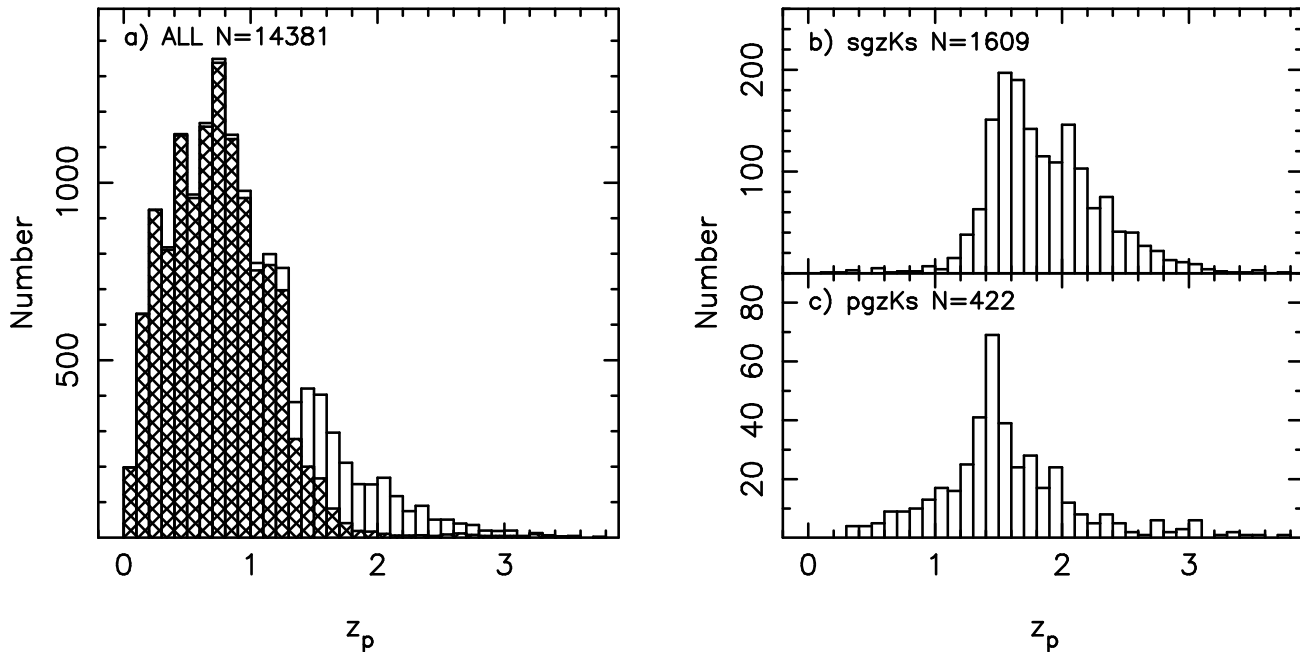


FIG. 3.— Photometric redshift distributions for the K -selected galaxies in our sample. The left panel shows the redshift distributions for all galaxies and all non-gzKs galaxies (cross-hatched). The top-right panel shows the redshift distributions of our sgzKs sample (1609 galaxies), the bottom-right panel shows the redshift distributions of pgzKs (422 galaxies).

high-mass galaxies, however predicted too many low-mass galaxies.

4. PHYSICAL PROPERTIES OF sgzKs

In this section, physical properties of sgzKs, such as stellar mass (M_*), SFR, and sSFR (SFR/M_*), are derived on the basis of the present photometric data.

4.1. Stellar Mass Estimates

In order to estimate the stellar mass (M_*) of sgzKs, we perform SED fitting of the multi-band photometry as described above with population synthesis models. The SED templates are generated with the SPS package developed by Bruzual & Charlot (2003). We assume an universal initial mass function (IMF) from Chabrier (2003). Masses derived assuming this IMF can be converted to Salpeter by adding 0.3 dex (Bundy et al. 2005). A grid of model templates spanning a range of star formation histories (parameterized as an exponential), ages, metallicities and dust content are used. The stellar mass-to-luminosity (M/L) ratios from the best-fit templates and the photometric redshifts (spectroscopic redshifts are adopted if available) from Section 2.3 are used to calculate the stellar mass. The histogram of the stellar mass of the sgzKs is shown in Figure 5(a). About 50% of the sgzKs in our sample have $M_* > 10^{11} M_\odot$, and the median stellar mass of sgzKs is $\sim 8.8 \times 10^{10} M_\odot$.

4.2. Star Formation Rates

The ultraviolet continuum can be used to estimate the luminosity from young stars and hence the SFR. We derive the SFR of each sgzKs based on its rest-frame 2800Å luminosity, which is calculated from the same best-fitting SED template as used in the estimation of the photometric redshift. Since our multi-band photometric data completely cover the rest-frame 2800Å

for the redshift range ($1.0 \lesssim z \lesssim 3.0$) of sgzKs, the estimated rest-frame 2800Å luminosity is a robust quantity, especially in the case where a galaxy is detected in both bands which straddle the rest-frame 2800Å. The color excess, $E(B - V)$, from the SED fitting is used to derive the dust-corrected UV luminosity. Then, we convert the dust-corrected rest-frame 2800Å luminosities into SFRs using the calibration by Kennicutt (1998): $\text{SFR} (M_\odot \text{ yr}^{-1}) = 1.4 \times 10^{-28} L_\nu (\text{erg s}^{-1} \text{ Hz}^{-1})$.

The SFR histogram of the sgzKs is shown in Figure 5(b). About 85% of sgzKs in our sample ($K_{\text{AB}} < 22$) have $\text{SFR} > 70 M_\odot \text{ yr}^{-1}$, and the median SFR is about $184 M_\odot \text{ yr}^{-1}$, which is similar to the values in Daddi et al. (2004) (with a typical SFR of $\sim 200 M_\odot \text{ yr}^{-1}$) and in Kong et al. (2006) (with a median SFR of $\sim 190 M_\odot \text{ yr}^{-1}$).

4.3. The SFR– M_* correlation

The existence of a correlation between star formation and stellar mass of galaxies at different redshifts ($0 < z < 2$) has been reported recently (Daddi et al. 2007; Elbaz et al. 2007; Pannella et al. 2009). To gain further insights into the nature of star formation at $1.4 < z < 3.0$, we show the SFR as a function of M_* in the four redshift bins in Figure 6. To examine in detail the stellar mass dependence of the SFR, we plot a good-fit line (dashed line) for galaxies with $M_* > 10^{10} M_\odot$ in each redshift panel. From this figure, we find a positive correlation between the SFR and stellar mass of sgzKs in the all four redshift bins.

In Figure 6(d), we overplot the correlation between the SFR and stellar mass for $z \sim 0.1$ galaxies in the Sloan Digital Sky Survey (SDSS; Brinchmann et al. 2004), $z \sim 1$ and $z \sim 2$ galaxies in the GOODS (Elbaz et al. 2007; Daddi et al. 2007), and $z \sim 0$ and $z \sim 1$ from Millennium model (Kitzbichler & White 2007). Figure 6(d) shows the slopes between the SFR and stellar mass of galaxies

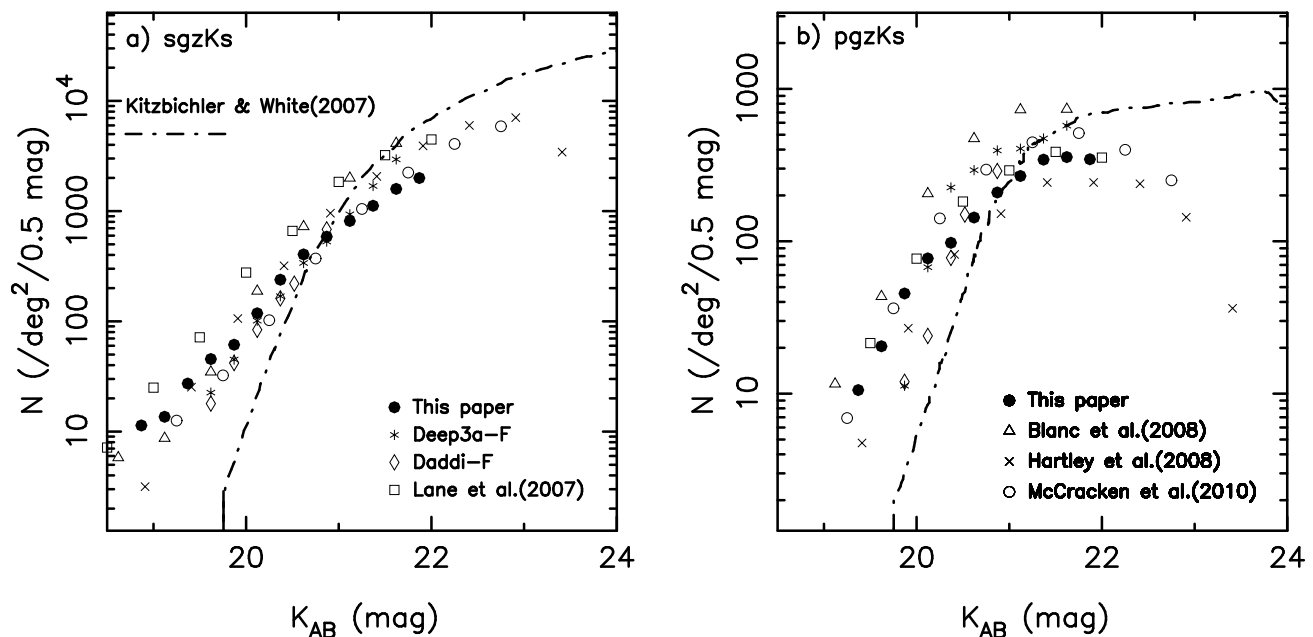


FIG. 4.— K -band differential number counts for star-forming galaxies (sgzKs) and passively evolving galaxies (pgzKs) at $z \sim 2$. For comparison, we have overplotted the number counts for $z \sim 2$ galaxies from the literature and the predictions of model of Kitzbichler & White (dot-dashed line). Left: sgzKs. Right: pgzKs.

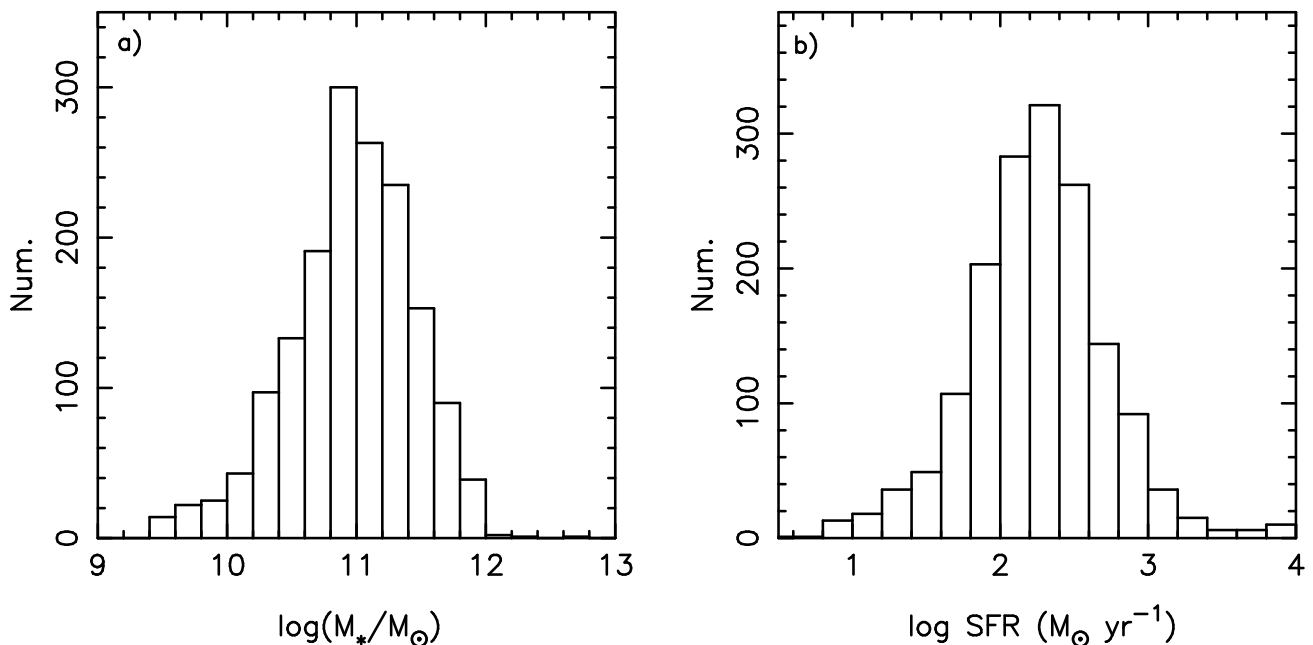


FIG. 5.— Stellar mass and star formation histogram of sgzKs in the EGS field. The left panel (a) is the plot for stellar mass, and the right panel (b) is the plot for star formation rate.

at different redshifts are very similar. On average, the SFR of galaxies on the SFR– M_* diagram increases with redshift at a fixed M_* , by a factor about 6 from $z \sim 0$ to $z \sim 1$, and a factor about 20 from $z \sim 0$ to $z \sim 2$. At fixed stellar mass, star-forming galaxies were much more active on average in the past. This is most likely due to a larger abundance of gas, depleted with passing of time (Daddi et al. 2007).

The Millennium model overlaps very well with the SDSS at $z \sim 0.1$ and predicts a slope very similar to the observed trend at different redshift bins. For $z \sim 1$, however, we find that at fixed stellar masses the model

predicts an increase of the SFR much below the observed trend. It seems that a major change required for models would be to increase the star formation efficiency (and thus the typical SFR) at all masses for star-forming galaxies at redshifts $z > 1$.

4.4. The $sSFR$ – M_* correlation

$sSFR$ is defined as the ratio of the current SFR to the current stellar mass, $sSFR = SFR/M_*$. Thus, higher values of the $sSFR$ indicate that a larger fraction of stars were formed recently, and it can be used to characterize the star formation history of galaxies.

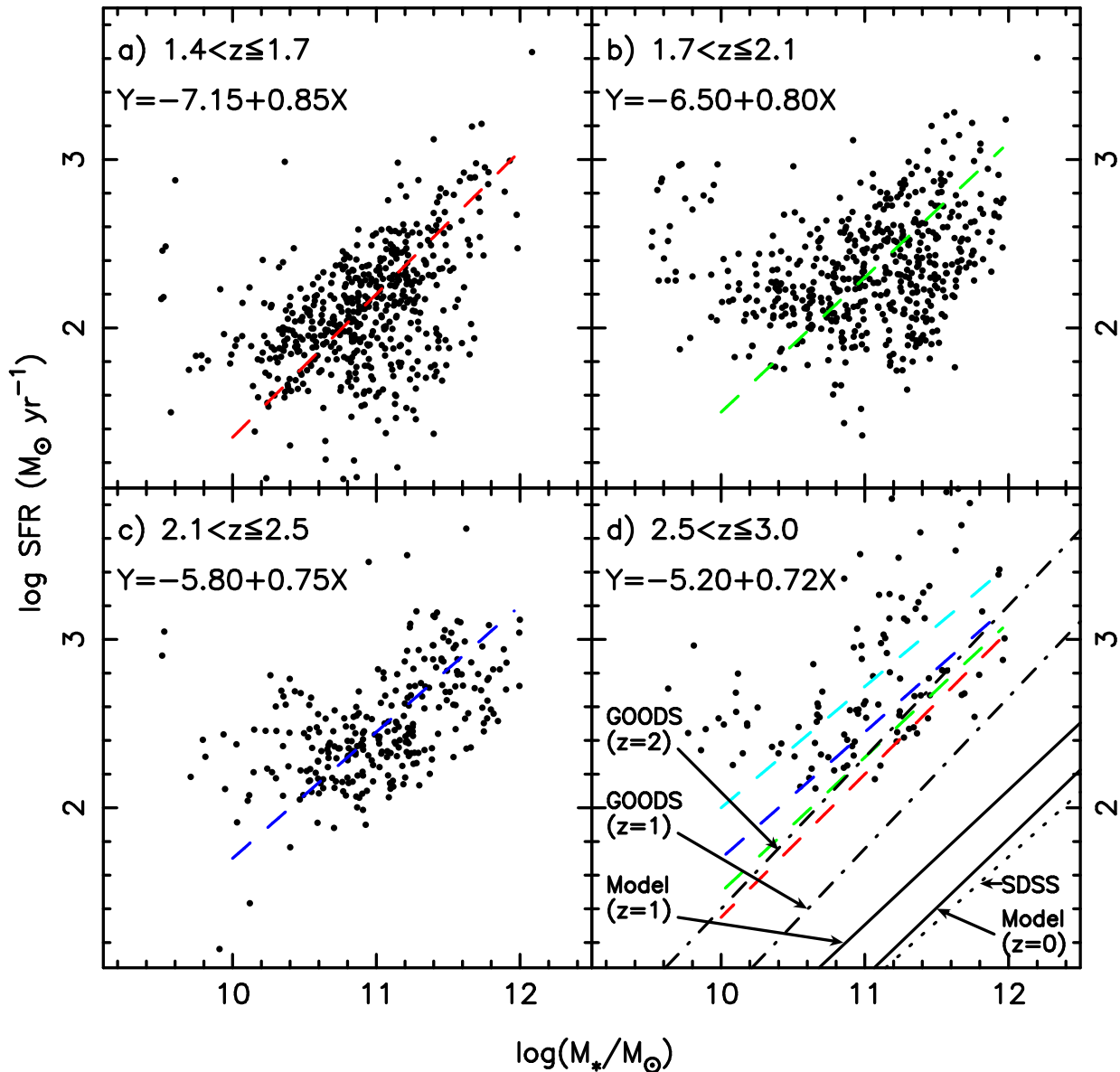


FIG. 6.— Relationship between stellar mass with SFR, for $z \sim 2$ star-forming galaxies in our sample for each redshift bin. Dashed lines and the equations (here $Y = \log \text{SFR}$, $X = \log (M_*/M_\odot)$) in each panel show the linear fit for galaxies with $M_* > 10^{10} M_\odot$. The dot-dashed lines are the $z = 2$ and $z = 1$ correlations from Daddi et al. (2007) and Elbaz et al. (2007). The solid lines show a prediction for $z = 0$ and $z = 1$ from the Millennium simulations (Kitzbichler & White 2007). The dashed line is the $z = 0.1$ correlation from SDSS (Brinchmann et al. 2004).

Figure 7 shows the sSFR as a function of stellar mass for the sgzKs in our sample, with the same four redshift bins as in Figure 6. The dashed lines in each panel represent a good fit between the sSFR and M_* for galaxies with $M_* > 10^{10} M_\odot$. In Figure 7(d), we overplot the correlation between the sSFR and stellar mass for $0.2 < z < 0.5$, $0.5 < z < 0.75$, and $0.75 < z < 1.0$ galaxies in Brinchmann & Ellis (2000).

From this figure, we find that the general shape of sSFR– M_* correlation is in good agreement with a similar study for $z < 1.0$ galaxies (Brinchmann & Ellis 2000), and the line of maximum sSFR runs parallel to lines of constant SFR. Furthermore, this sSFR is generally increasing with increasing redshift for all stellar masses, suggesting that star formation contributes more to the growth of low-mass galaxies than to the growth of high-mass galaxies. Finally, the most massive galaxies have

the lowest sSFR at redshift $z < 2$; they formed their stars earlier and more rapidly than their low-mass counterparts. This is in agreement with the downsizing scenario.

5. MORPHOLOGY

The morphology of a galaxy reflects its dynamical history and evolution. For instance, different Hubble types are associated with different star formation histories and different patterns of motion of stars and gas. Furthermore, galaxy morphology correlates with a range of physical properties in galaxies, such as stellar mass, luminosity, size, velocity dispersion, concentration, and, particularly, color; this suggests that morphology is crucial in our understanding of the formation and evolution of galaxies (Fang et al. 2009; Kong et al. 2009).

With the advent of the new WFC3 on board *HST*,

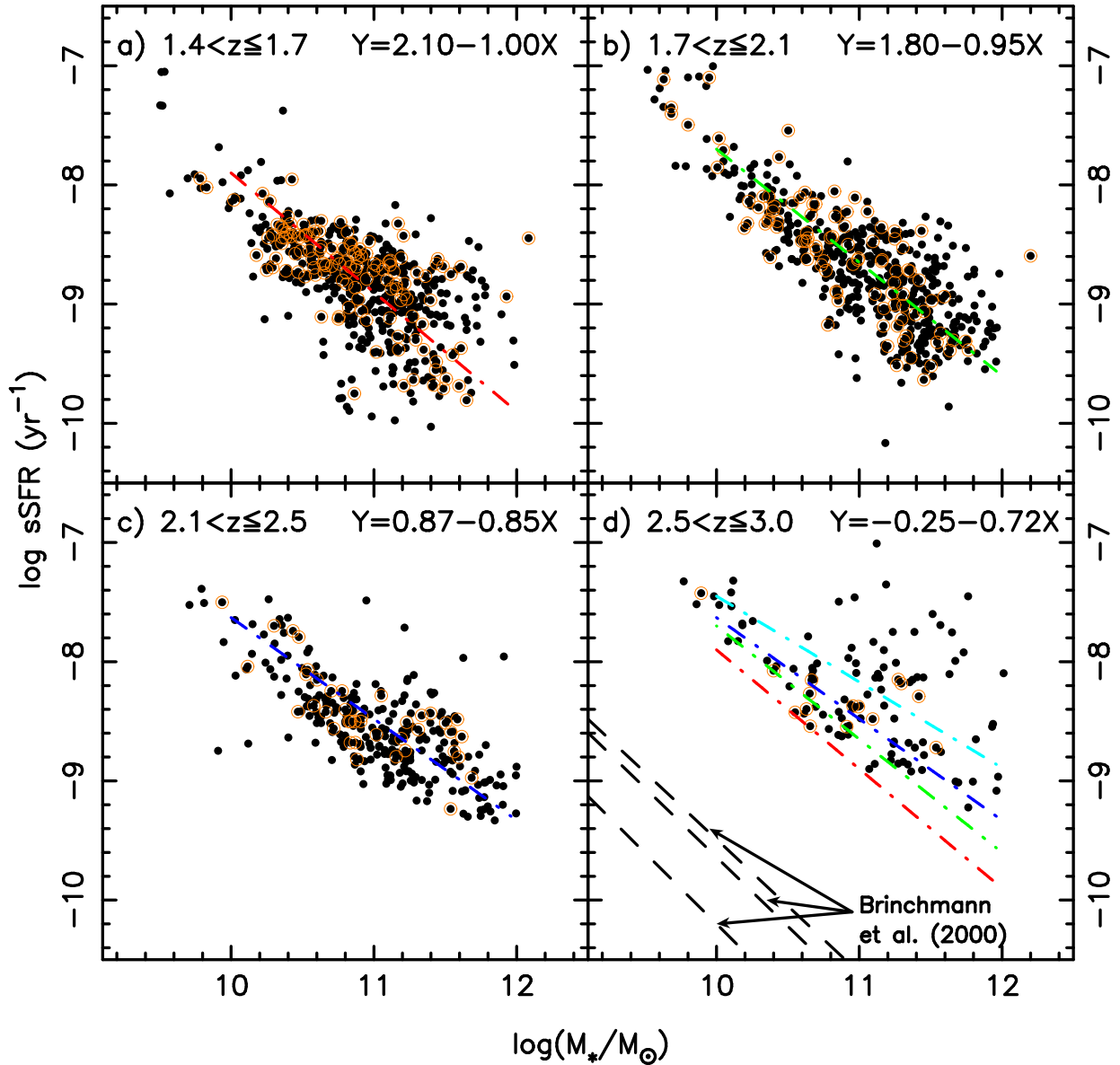


FIG. 7.— Specific star formation rate (sSFR) as a function of stellar mass for szgKs in the EGS. The dashed lines correspond to the best fit to the four redshift ranges indicated. The three dashed lines from Brinchmann & Ellis (2000) were overplotted in the bottom-left panel (d). The sample of szgKs with open circles from the overlapping area between NMBS and AEGIS.

with its vastly improved sensitivity and resolution compared to NICMOS, it has become possible to analyze the rest-frame optical structure of $z \sim 2$ galaxies with an unprecedented level of detail. To describe clearly the morphologies of both szgKs and pgzKs, we have performed nonparametric measures of galaxy morphology by using data from *HST* WFC3/H(F160W) imaging (Groggin et al. 2011; Koekemoer et al. 2011), such as Gini coefficient (the relative distribution of the galaxy pixel flux values, or G) and M_{20} (the second-order moment of the brightest 20% of the galaxy’s flux). Early-type galaxies have higher G and lower M_{20} , while late-type galaxies have lower G and higher M_{20} . Combining G and M_{20} permits classifying different galaxy population effectively (Lotz et al. 2006; Kong et al. 2009).

In Figure 8, the blue squares and red circles represent the morphological distribution of 173 szgKs and 50 pgzKs (these sources have H -band counterparts) in the

rest-frame wavelength $\sim 5300\text{\AA}$, respectively. The distribution of gzKs is very similar to that of local galaxies (E-Sd) in Lotz et al. 2004, with pgzKs showing high G and low M_{20} , and szgKs with lower G and higher M_{20} values. This figure clearly illustrates the morphological variety present at $z \sim 2$. The median (G , M_{20}) values for szgKs are (0.49, -1.48) in the rest-frame optical band, while pgzKs are (0.64, -1.74). A sample of 73 local ULIRGs ($z < 0.2$) is also shown in this diagram (Lotz et al. 2004), indicated as empty stars, using data from *HST* WFPC 2/F814W imaging (Borne et al. 2000). The solid diamonds and triangles in Figure 8 represent the starburst-dominated sources at $z \sim 2$ from Bussmann et al. (2011) and Förster Schreiber et al. (2011), respectively; their G and M_{20} values were derived from NICMOS/F160W images, corresponding to the rest-frame optical wavelength. The dashed line ($G = 0.4M_{20} + 0.9$) in this figure is drawn qualitatively at rest-frame optical band ($\sim 5300\text{\AA}$; Buss-

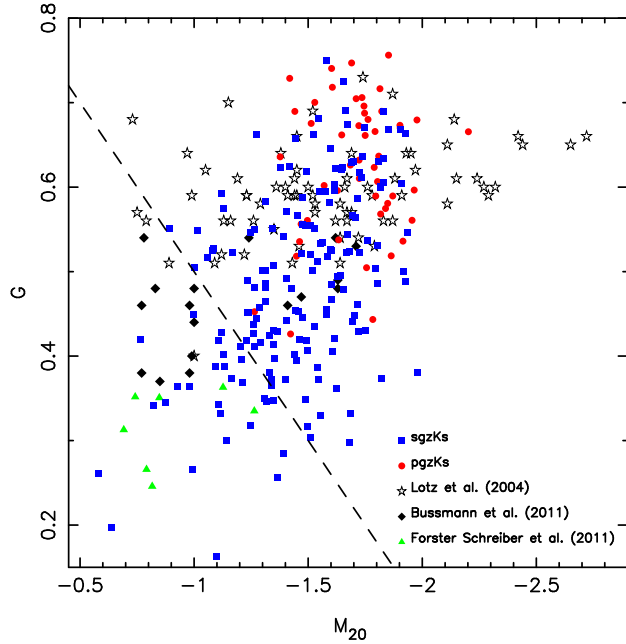


FIG. 8.— M_{20} vs. Gini coefficient (G) for sgzKs, pgzKs, $z \sim 2$ ULIRGs and local ULIRGs (empty stars; Lotz et al. 2004). The dashed line is defined as $G = 0.4M_{20} + 0.9$ (Bussmann et al. 2011). Filled blue squares and red circles represent the morphological distribution of 173 sgzKs and 50 pgzKs in our sample, respectively, which are matched in *HST*/WFC3 H -band. The starburst-dominated sources at $z \sim 2$ from Förster Schreiber et al. (2011) and Bussmann et al. (2011) are shown as filled triangles and diamonds, respectively, with G and M_{20} derived from *HST* NICMOS/F160W images.

mann et al. 2011). Galaxies with $G < 0.4M_{20} + 0.9$ have diffuse structures or multiple bright nuclei in appearance. Objects with $G > 0.4M_{20} + 0.9$ and $-1.6 < M_{20}$ can be irregular, often with a bright nucleus with tidal tail or fainter knots. As for sources with $G > 0.4M_{20} + 0.9$ and $M_{20} < -1.6$, they are relatively smooth with a single nucleus. From Figure 8, we find that star-forming galaxies at high redshift not only have diffuse structures, similar to starburst-dominated ULIRGs at $z \sim 2$ with lower G and higher M_{20} values, but also have single-object morphologies (higher G and lower M_{20}). Moreover, the distribution of M_{20} of sgzKs is mainly located in the range from -1.0 to -1.8 ; these features of morphologies are consistent with expectations from simulations of major mergers during the beginning and end stages, respectively, of the phase of the merger when the SFR peaks and begins to turn over (Lotz et al. 2008).

Figures 9 and 10 show the *HST*/WFC3 J - and H -band stamp images for a subset of six sgzKs and six pgzKs, respectively. Their rest-frame optical morphologies for sgzKs are very diversified including string-like, extended/diffused, and even early-type spiral morphologies, while pgzKs are relatively smooth and compact, implying that there are different formation process for these galaxies. Therefore, we conclude that the population of Hubble sequence galaxies roughly matches that of the peculiars sometime between $z = 1.5$ – 2 .

6. FRACTION OF AGNS

Mid-IR photometry has been proven to be a robust and efficient tool to select AGNs without prior information (e.g., Lacy et al. 2004; Stern et al. 2005; Donley

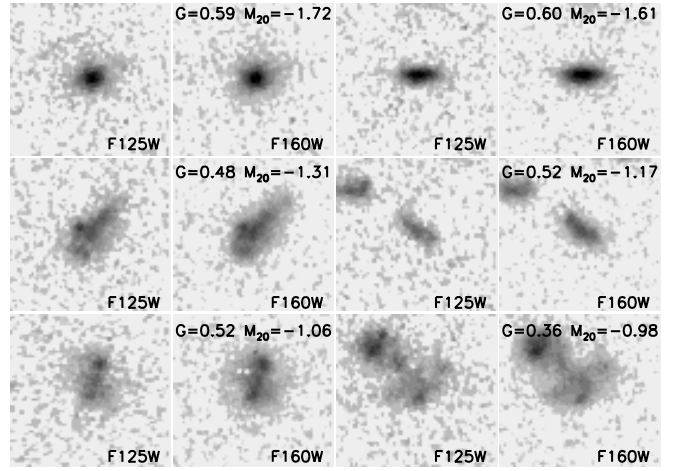


FIG. 9.— *HST*/WFC3 J - and H -band images of six sgzKs in the EGS. Top: $M_{20} < -1.60$, middle: $-1.60 < M_{20} < -1.10$, bottom: $M_{20} > -1.10$. Values of G and M_{20} are shown in each H -band image. All images are in negative gray scale and are 4×4 arcsec² in size.

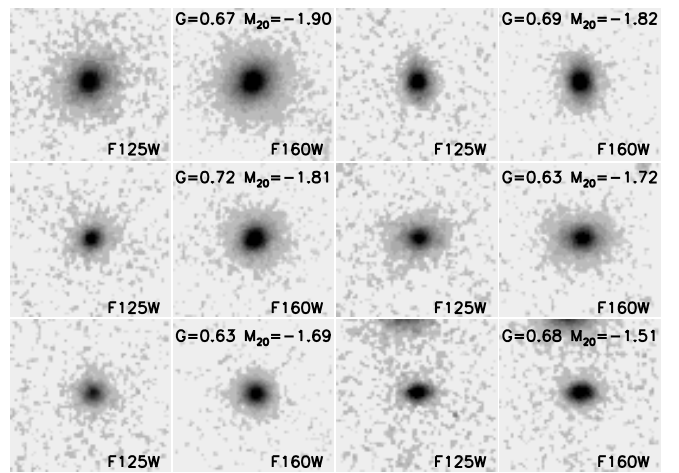


FIG. 10.— *HST*/WFC3 J - and H -band images of six pgzKs in the EGS. Top: $M_{20} < -1.81$, middle: $-1.81 < M_{20} < -1.70$, bottom: $M_{20} > -1.70$. Values of G and M_{20} are shown in each H -band image. All images are in negative gray scale and are 4×4 arcsec² in size.

et al. 2008), as their properties at these wavelengths are typically very different from those of stars and galaxies. There have been several studies of AGN selection using mid-IR color or other IR properties. In this section, two different AGN selection methods are employed, to identify AGNs in our gzK sample. The first one is based on the IRAC band color criteria of Stern et al. (2005). The second method is based on Mid-IR spectral index (Barmby et al. 2006; Park et al. 2010).

6.1. Mid-IR colors

Figure 11 shows the mid-IR color space of the EGS survey along with the Stern et al. (2005) AGN selection criterion (green dot-dashed lines). Small dots represent the distribution of Mid-IR color for sources detected in all four IRAC channels in the AEGIS field; they have very similar $[3.6] - [4.5]$ colors, as this is dominated by their stellar emission. Six hundred and twelve sgzKs in our sample are detected in all the four IRAC channels and are plotted as blue open circles. One hundred and

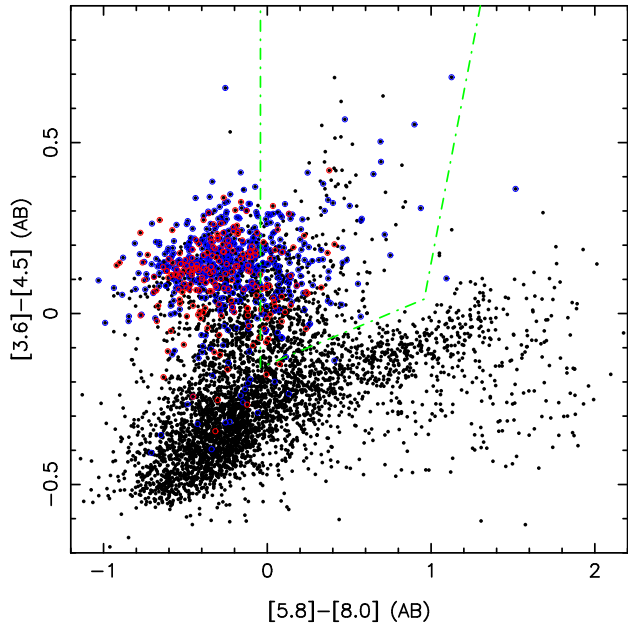


FIG. 11.— IRAC band color-color diagram of galaxies in the EGS field. Dot-dashed lines indicate the boundaries of the AGN selection wedges from Stern et al. (2005). Small points represent all galaxies, sgzKs are denoted by blue open circles, and pgzKs are denoted by red open circles.

twenty-two of them can be selected as AGN candidates by the mid-IR selection criterion of Stern et al. (2005). Two hundred and sixteen pgzKs in our sample are detected in all the four IRAC channels and plotted as red open circles. Thirty-five of them are AGN candidates. Therefore, using the mid-IR AGN selection criterion, $\sim 20\%$ of sgzKs and $\sim 16\%$ of pgzKs are classified as AGNs, respectively.

The AGN selection criterion from Stern et al. (2005) were based on the spectroscopic sample of the AGN and Galaxy Evolution Survey, most of which have redshift $z < 0.6$. Their mid-IR color criterion is reliable for classifying AGNs and galaxies at low redshift. In contrast, observations and templates suggest that a high degree of stellar contamination is unavoidable when the color selection technique is applied to deeper samples (Barmby et al. 2006; Donley et al. 2008; Georgantopoulos et al. 2008; Assef et al. 2010). The redshift of sgzKs and pgzKs in our sample is $z \sim 2$; with much deeper IRAC data, we will classify AGNs from normal galaxies with the mid-IR spectral index method in the next subsection.

6.2. Mid-IR spectral index

The slope of a galaxy SED in the infrared can be characterized by a power-law behavior of flux density with frequency $f_\nu \propto \nu^\alpha$. AGN SEDs often follow a negative-sloping (red) power-law, which may arise from either thermal or non-thermal emission originating near the central region. In contrast, stellar-dominated sources at redshift $z \lesssim 2$ generally exhibit positive (blue) IRAC power law emission. For this reason, mid-IR power-law α of galaxies have been proposed and used as classification criteria for AGNs and normal galaxies, with a small level of galaxy contamination.

In this paper, the IRAC fluxes for each gzKs, covering the 3.6–8.0 μm range, are fitted with a power law, α .

The α value is only accepted if the χ^2 probability fit is $P_{\chi^2} > 0.1$. Galaxies fitted well with a power-law SED are further classified as red or blue. A limit of $\alpha \lesssim -0.5$, following Donley et al. (2008) and Park et al. (2010), is chosen to classify gzKs as AGNs. The criterion reveals that the fraction of AGNs in our sample is $\sim 10\%$. In the meantime, we also check the X-ray luminosities of these AGN candidates (if they have X-ray counterparts), and the result shows that most of these objects have $L_{0.5-10 \text{ keV}} > 10^{41} \text{ erg s}^{-1}$.

7. SUMMARY

In this paper, we have described the construction of a sample of gzKs (correspond to the BzKs of Daddi et al. 2004) within the AEGIS. With this field’s unique combination of area and depth at almost every waveband observable, we analyze the photometric redshifts, number counts, SFRs, sSFRs, stellar masses, morphologies, and the fraction of AGNs of gzKs in the AEGIS. Our main conclusions are as follows.

1. We identify a sample of 2031 gzKs including 1609 star-forming galaxies, with $gzK = (z - K)_{\text{AB}} - 1.4(g - z)_{\text{AB}} \geq 0.2$ and 422 passively evolving galaxies with $gzK < 0.2$ and $(z - K)_{\text{AB}} > 2.7$, to a limit $K_{\text{AB}} < 22$. The surface density of sgzKs+pgzKs is $\sim 1.28 \text{ arcmin}^{-2}$. Of the sgzK galaxies, 83.2% lie in the range $1.4 \leq z \leq 2.5$, while 8.5% are at $z < 1.4$ and 8.3% at $z > 2.5$. For pgzK galaxies, there is a considerable fraction (12.8%) of objects at low redshift ($z < 1.0$). The z_p median values of both sgzKs and pgzKs are 1.8 and 1.5, respectively.

2. For a sample selected at $K_{\text{AB}} < 22.0$, 2989 spectroscopic redshift of field galaxies (including 35 LBGs at $z \sim 3$ and 14 ULIRGs at $z \sim 2$), we reach an average redshift accuracy of $\delta z / (1 + z_s) = -0.014$ with the normalized median absolute deviation (σ_{NMAD}) of 0.032. Only 4.3% galaxies have $(z_p - z_s) / (1 + z_s) > 0.1$. We also compare our photometric redshifts with NMBS photometric redshifts in the AEGIS field; they are in good agreement.

3. Similar to the findings in other literatures, our counts of passively evolving galaxies turn over at $K_{\text{AB}} \sim 21.0$ and both the number of faint and bright sources (including sgzKs and pgzKs) in our catalogs exceed the predictions of a recent semi-analytic model of galaxy formation, implying that a more successful model must have to explain this diversity in the future.

4. Based on the reddening-corrected UV luminosities and SED fitting of the multi-band photometry, we find that gzK -selected star-forming galaxies have a median SFR and stellar mass of $\sim 184 M_\odot \text{ yr}^{-1}$ and $\sim 8.8 \times 10^{10} M_\odot$, respectively. Moreover, we also find that the SFR and sSFR of sgzKs increases with redshift at all masses, suggesting that star-forming galaxies were much more active on average in the past. Comparing to the predictions of the Millennium model, there is a major change required for models in order to increase the star formation efficiency at all masses for star-forming galaxies at redshifts $z > 1$.

5. We also study the morphological properties of gzKs in our sample, employing data from *HST* WFC3/F160W imaging within the EGS field. We derived the median (G , M_{20}) values for sgzKs and pgzKs are (0.49, -1.48) and (0.64, -1.74) in the rest-frame optical band, respectively. Moreover, we find that morphologies of $z \sim 2$ galaxies in our sample are complex and varied: from compact,

apparently early-type galaxies to large star-forming systems superficially similar to pure disk or irregular galaxies, implying that there are different formation processes for these galaxies. We conclude that the population of Hubble sequence galaxies roughly matches that of the peculiars sometime between $z = 1.5$ – 2 .

6. For the fraction of AGNs in the gzKs, we compared the power-law selection technique with mid-infrared color selection, and we find that 82 sources with $\alpha \leq -0.5$, corresponding to the fraction of AGNs, is $\sim 10\%$ in our sample of 828 gzK galaxies with four IRAC bands. In the meantime, we also check the X-ray luminosities of these sources (if they have X-ray counterparts); the result shows that most of these objects have $L_{0.5-10 \text{ keV}} > 10^{41} \text{ erg s}^{-1}$.

We thank the anonymous referee for valuable com-

ments and suggestions that have improved the paper. We thank J.-S. Huang and H. J. McCracken for helpful suggestions and discussions. This study makes use of data from AEGIS, a multi-wavelength sky survey conducted with the *Chandra*, *GALEX*, *Hubble*, Keck, CFHT, MMT, Subaru, Palomar, *Spitzer*, VLA, and other telescopes and supported in part by the NSF, NASA, and the STFC. This work is also based on observations taken by the CANDELS Multi-Cycle Treasury Program with the NASA/ESA *HST*, which is operated by the Association of Universities for Research in Astronomy, Inc., under NASA contract NAS5-26555. The work is supported by the National Natural Science Foundation of China (NSFC, No. 10873012), the Open Research Program of Key Laboratory for the Structure and Evolution of Celestial Objects, CAS, and Chinese Universities Scientific Fund (CUSF).

REFERENCES

- Abraham, R. G., Glazebrook, K., McCarthy, P. J., et al. 2004, *AJ*, 127, 2455
- Arnouts, S., Walcher, C. J., Le Fèvre, O., et al. 2007, *A&A*, 476, 137
- Assef, R. J., Kochanek, C. S., Brodwin, M., et al. 2010, *ApJ*, 713, 970
- Balogh, M. L., McGee, S. L., Wilman, D., et al. 2009, *MNRAS*, 398, 754
- Barmby, P., Alonso-Herrero, A., Donley, J. L., et al. 2006, *ApJ*, 642, 126
- Barmby, P., Huang, J.-S., Ashby, M. L. N., et al. 2008, *ApJS*, 177, 431
- Bertin, E., & Arnouts, S. 1996, *A&AS*, 117, 393
- Blanc, G. A., Lira, P., Barrientos, L. F., et al. 2008, *ApJ*, 681, 1099
- Bolzonella, M., Miralles, J.-M., & Pelló, R. 2000, *A&A*, 363, 476
- Borne, K. D., Bushouse, H., Lucas, R. A., & Colina, L. 2000, *ApJ*, 529, 77
- Brammer, G. B., & van Dokkum, P. G. 2007, *ApJ*, 654, L107
- Brammer, G. B., Whitaker, K. E., van Dokkum, P. G., et al. 2009, *ApJ*, 706, L173
- Brammer, G. B., Whitaker, K. E., van Dokkum, P. G., et al. 2011, *ApJ*, 739, 24
- Brinchmann, J., Charlot, S., White, S. D. M., et al. 2004, *MNRAS*, 351, 1151
- Brinchmann, J., & Ellis, R. S. 2000, *ApJ*, 536, L77
- Bruzual, G., & Charlot, S. 2003, *MNRAS*, 344, 1000
- Bundy, K., Ellis, R. S., & Conselice, C. J. 2005, *ApJ*, 625, 621
- Bundy, K., Ellis, R. S., Conselice, C. J., et al. 2006, *ApJ*, 651, 120
- Bussmann, R. S., Dey, A., Lotz, J., et al. 2011, *ApJ*, 733, 21
- Chabrier, G. 2003, *PASP*, 115, 763
- Chapman, S. C., Blain, A. W., Smail, I., & Ivison, R. J. 2005, *ApJ*, 622, 772
- Cimatti, A., Daddi, E., Mignoli, M., et al. 2002, *A&A*, 381, L68
- Conselice, C. J., Bundy, K., Trujillo, I., et al. 2007, *MNRAS*, 381, 962
- Cowie, L. L., Songaila, A., Hu, E. M., et al. 1994, *ApJ*, 432, L83
- Daddi, E., Cimatti, A., Renzini, A., et al. 2004, *ApJ*, 617, 746
- Daddi, E., Dickinson, M., Morrison, G., et al. 2007, *ApJ*, 670, 156
- Davis, M., Guhathakurta, P., Konidaris, N. P., et al. 2007, *ApJ*, 660, L1
- Desai, V., Soifer, B. T., Dey, A., et al. 2009, *ApJ*, 700, 1190
- Dey, A., Soifer, B. T., Desai, V., et al. 2008, *ApJ*, 677, 943
- Dickinson, M., Papovich, C., Ferguson, H. C., & Budavári, T. 2003, *ApJ*, 587, 25
- Donley, J. L., Rieke, G. H., Pérez-González, P. G., & Barro, G. 2008, *ApJ*, 687, 111
- Drory, N., Bundy, K., Leauthaud, A., et al. 2009, *ApJ*, 707, 1595
- Drory, N., Salvato, M., Gabasch, A., et al. 2005, *ApJ*, 619, L131
- Dunne, L., Ivison, R. J., Maddox, S., et al. 2009, *MNRAS*, 394, 3
- Elbaz, D., Daddi, E., Le Borgne, D., et al. 2007, *A&A*, 468, 33
- Fadda, D., Yan, L., Lagache, G., et al. 2010, *ApJ*, 719, 425
- Fang, G.-W., Huang, J.-S., Kong, X., et al. 2011, *ApJ*, submitted
- Fang, G.-W., Kong, X., & Wang, M. 2009, *Research in Astronomy and Astrophysics*, 9, 59
- Farrah, D., Lonsdale, C. J., Weedman, D. W., et al. 2008, *ApJ*, 677, 957
- Fiolet, N., Omont, A., Lagache, G., et al. 2010, *A&A*, 524, A33
- Fontana, A., Donnarumma, I., Vanzella, E., et al. 2003, *ApJ*, 594, L9
- Fontana, A., Salimbeni, S., Grazian, A., et al. 2006, *A&A*, 459, 745
- Förster Schreiber, N. M., Shapley, A. E., Erb, D. K., et al. 2011, *ApJ*, 731, 65
- Franx, M., Labbé, I., Rudnick, G., et al. 2003, *ApJ*, 587, L79
- Furusawa, J., Sekiguchi, K., Takata, T., et al. 2011, *ApJ*, 727, 111
- Georgantopoulos, I., Georgakakis, A., Rowan-Robinson, M., & Rovilos, E. 2008, *A&A*, 484, 671
- Grogin, N. A., Kocevski, D. D., Faber, S. M., et al. 2011, *ApJS*, 197, 35
- Hartley, W. G., Lane, K. P., Almaini, O., et al. 2008, *MNRAS*, 391, 1301
- Huang, J.-S., Faber, S. M., Daddi, E., et al. 2009, *ApJ*, 700, 183
- Kennicutt, R. C., Jr. 1998, *ARA&A*, 36, 189
- Kitzbichler, M. G., & White, S. D. M. 2007, *MNRAS*, 376, 2
- Koekemoer, A. M., Faber, S. M., Ferguson, H. C., et al. 2011, *ApJS*, 197, 36
- Kong, X., Daddi, E., Arimoto, N., et al. 2006, *ApJ*, 638, 72
- Kong, X., Fang, G.-W., Arimoto, N., & Wang, M. 2009, *ApJ*, 702, 1458
- Labbé, I., Huang, J., Franx, M., et al. 2005, *ApJ*, 624, L81
- Lacy, M., Storrie-Lombardi, L. J., Sajina, A., et al. 2004, *ApJS*, 154, 166
- Laird, E. S., Nandra, K., Georgakakis, A., et al. 2009, *ApJS*, 180, 102
- Lane, K. P., Almaini, O., Foucaud, S., et al. 2007, *MNRAS*, 379, L25
- Lotz, J. M., Jonsson, P., Cox, T. J., & Primack, J. R. 2008, *MNRAS*, 391, 1137
- Lotz, J. M., Madau, P., Giavalisco, M., Primack, J., & Ferguson, H. C. 2006, *ApJ*, 636, 592
- Lotz, J. M., Primack, J., & Madau, P. 2004, *AJ*, 128, 163
- McCracken, H. J., Capak, P., Salvato, M., et al. 2010, *ApJ*, 708, 202
- Nandra, K., Laird, E. S., Adelberger, K., et al. 2005, *MNRAS*, 356, 568
- Noeske, K. G., Weiner, B. J., Faber, S. M., et al. 2007, *ApJ*, 660, L43
- Onodera, M., Arimoto, N., Daddi, E., et al. 2010, *ApJ*, 715, 385
- Pannella, M., Carilli, C. L., Daddi, E., et al. 2009, *ApJ*, 698, L116
- Papovich, C., Moustakas, L. A., Dickinson, M., et al. 2006, *ApJ*, 640, 92
- Park, S. Q., Barmby, P., Willner, S. P., et al. 2010, *ApJ*, 717, 1181
- Patel, S. G., Kelson, D. D., Holden, B. P., Franx, M., & Illingworth, G. D. 2011, *ApJ*, 735, 53

- Pérez-González, P. G., Rieke, G. H., Villar, V., et al. 2008, *ApJ*, 675, 234
- Pozzetti, L., Bolzonella, M., Lamareille, F., et al. 2007, *A&A*, 474, 443
- Quadri, R. F., Williams, R. J., Lee, K.-S., et al. 2008, *ApJ*, 685, L1
- Richards, G. T., Strauss, M. A., Fan, X., et al. 2006, *AJ*, 131, 2766
- Scoville, N., Aussel, H., Brusa, M., et al. 2007, *ApJS*, 172, 1
- Steidel, C. C., Adelberger, K. L., Shapley, A. E., et al. 2003, *ApJ*, 592, 728
- Steidel, C. C., Shapley, A. E., Pettini, M., et al. 2004, *ApJ*, 604, 534
- Stern, D., Eisenhardt, P., Gorjian, V., et al. 2005, *ApJ*, 631, 163
- Stetson, P. B. 1987, *PASP*, 99, 191
- Szomoru, D., Franx, M., Bouwens, R. J., et al. 2011, *ApJ*, 735, L22
- van Dokkum, P. G., Franx, M., Förster Schreiber, N. M., et al. 2004, *ApJ*, 611, 703
- van Dokkum, P. G., Labbé, I., Marchesini, D., et al. 2009, *PASP*, 121, 2
- van Dokkum, P. G., Quadri, R., Marchesini, D., et al. 2006, *ApJ*, 638, L59
- van Dokkum, P. G., Whitaker, K. E., Brammer, G., et al. 2010, *ApJ*, 709, 1018
- Whitaker, K. E., Labbé, I., van Dokkum, P. G., et al. 2011, *ApJ*, 735, 86
- Whitaker, K. E., van Dokkum, P. G., Brammer, G., et al. 2010, *ApJ*, 719, 1715
- Williams, R. J., Quadri, R. F., Franx, M., van Dokkum, P. G., & Labbé, I. 2009, *ApJ*, 691, 1879
- Williams, R. J., Quadri, R. F., Franx, M., et al. 2010, *ApJ*, 713, 738
- Wolf, C., Aragón-Salamanca, A., Balogh, M., et al. 2009, *MNRAS*, 393, 1302
- Wuyts, S., Labbé, I., Franx, M., et al. 2007, *ApJ*, 655, 51
- Yoshikawa, T., Akiyama, M., Kajisawa, M., et al. 2010, *ApJ*, 718, 112